CRYSTAL GROWTH & DESIGN

pubs.acs.org/crystal

Article

Target Configuration Effect on Microstructures and Properties of Vertically Aligned Nanocomposites

Lizabeth Quigley, Jianan Shen, Juanjuan Lu, Claire A. Mihalko, James P. Barnard, Yizhi Zhang, Nirali A. Bhatt, Katrina Evancho, Raktim Sarma, Aleem Siddiqui, and Haiyan Wang*

Cite This: *Cryst. Growth Des.* 2024, 24, 8929−8936

Read Online

ACCESS | Metrics & More | Article Recommendations | Supporting Information

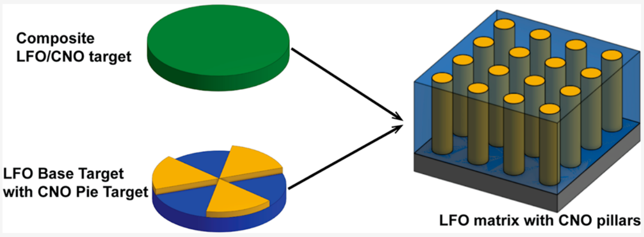

ABSTRACT: Vertically aligned nanocomposites (VANs) are unique thin films with vertical nanostructures embedded in a matrix material, allowing for the integration of two distinct materials. These nanocomposites offer novel combined physical properties, such as nanocomposite-based multiferroics and strongly coupled physical properties, such as magneto-optic coupling. Much work has been conducted in exploring different two-phase combinations and various processing conditions to achieve novel tunable properties that cannot be obtained by any single-phase material alone. In this work, the target configuration effects are explored for the growth of $LaFeO_3$−$CoNi_2O_4$ VANs. Both mixed and pie-shaped targets are utilized to compare the target configuration effects on the phase separation, morphology tuning, and their resulting physical properties, including optical and magnetic properties. This work suggests that the target configuration is another important parameter for achieving the desired VAN morphology and can be used to design different two-phase VANs with tailorable properties.

■ INTRODUCTION

Vertically aligned nanocomposites (VANs) have the ability to self-assemble into unique morphologies which has attracted significant research interest.[1−5] This ability has allowed for the creation of films with novel material compositions and anisotropic physical properties. These materials form a matrix of one material and vertical pillars of the other, each chosen for their specific electrical, optical, and magnetic properties.[1−5] The material selection also enables possible property couplings between the matrix and the pillars. One example includes ferroelectric and ferromagnetic (FM) materials forming new nanocomposite-based multiferroic films while another example is the enhancement of exchange bias properties through antiferromagnetic (AFM) and ferromagnetic (FM) materials through AFM-FM coupling at the interfaces.[1,6−9] In addition, the microstructures and properties of the VAN materials can easily be tuned by adjusting the deposition parameters, such as oxygen partial pressure, laser energy, deposition frequency, film thickness, substrate choice, and more.[2−5,10] Notably, even small changes in the composition can greatly affect the microstructures and properties.[2−5]

An important but underinvestigated processing parameter for VAN growth is the target selection and configuration. There are several popular target configurations in use for VAN depositions. Composite targets have all of the components for the matrix and the pillar mixed together in a predetermined ratio. These targets are widely used for the growth of oxide−oxide, oxide-metal, or nitride-metal VAN systems.[11−16] Another one is using a base target with a metal strip for most of the oxide-metal and nitride-metal VAN demonstrations.[17−20] Separated targets have the two different materials made into separate targets, and during the deposition, the laser pulses are directed at each target sequentially.[21,22] Finally, pie-shaped targets also include the matrix and pillar material being made into different targets, but these are pasted together in an alternating fashion for VAN deposition.[23−25] Each target configuration changes how the deposition is completed and allows for different variations in the material ratios. For example, the composite target cannot have the ratio of the two materials varied because the composition is fixed during target sintering. Separated target styles can be adjusted by changing the duration of the laser exposure on each material. The different types of separated targets can also be reused for different material compositions, while the composite target can only be used for one specific VAN growth. Despite the strong impacts of the target configurations on VAN growth, such comparison studies on the different target configurations are limited.

Received: July 10, 2024
Revised: September 29, 2024
Accepted: September 30, 2024
Published: October 9, 2024

https://doi.org/10.1021/acs.cgd.4c00958
Cryst. Growth Des. 2024, 24, 8929−8936

In this work, two target configurations were adopted for an oxide−oxide VAN growth to explore the impact of the target configuration on the overall VAN two-phase morphology and their resulting physical properties. Specifically, the oxide−oxide VAN based on $LaFeO_3$ (LFO) matrix with $CoNi_2O_4$ (CNO) is proposed for this study. LFO is a FM and dielectric material with a narrow band gap of 2.08 eV, while CNO is predicted to be metallic and ferrimagnetic. Combining them into the VAN form could result in an all-oxide anisotropic optical and magnetic metamaterials, a Mott insulating LFO matrix with conducting CNO pillars while overall providing strong magnetic anisotropy.[26−30] Considering the oxide materials as the two phases, further oxidization cannot occur to reduce the magnetic properties, and including optical properties, into the film increases the film's capabilities in future device applications. Two different configurations of targets were explored for growing the VAN system, as shown in Figure 1.

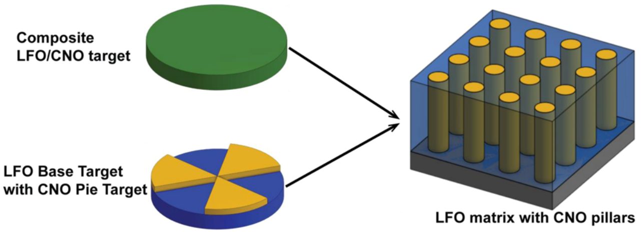

Figure 1. Proposed LFO−CNO VAN thin films using both a composite LFO/CNO target and a separated LFO base with CNO "pie slices". It was expected that both target configurations would result in a similar pillar-in-matrix film.

One was a composite target with a 1:1 ratio between LFO and CNO being made, while the other target was a pie-shaped target combining LFO and CNO. In other words, the first target is mixed powder form, while the second target is with the LFO and CNO separated, specifically with the CNO being made from smaller sections. During deposition, the ratio between the material phases was kept at 1:1 for both cases. The depositions were carried out with a laser frequency of both 2 and 10 Hz for both target configurations, allowing for more variation within the films, such as the pillar size and density. Depositions at a laser frequency of 5 Hz were also conducted, and data for the 5 Hz sample can be found in the Supporting Information in Figures S4−S8. Besides the target configuration and the laser frequency used, other deposition parameters were kept consistent throughout all depositions. After deposition, the samples were characterized through scanning transmission electron microscopy (STEM), energy dispersive X-ray spectroscopy (EDS), X-ray diffraction (XRD), and magnetic and optical measurements to explore the impacts on the target configuration on the overall phase distribution, morphology, and properties of the resulting VANs.

■ EXPERIMENTAL SECTION

The composite target was prepared by mixing NiO, La_2O_3, Fe_2O_3, and Co_3O_4 in portions that allowed for a 1:1 molar ratio of $LaFeO_3$ to $CoNi_2O_4$. The powders were mixed in a ball miller for 24 h followed by another hour of manual milling. The powders were then pressed into a target and sintered for 10 h at 1000 °C. The individual $LaFeO_3$ target was made from Fe_2O_3 and La_2O_3 powders. It was ball milled for 10 h before being pressed into a target and sintered at 1000 °C for 10 h. Manual milling did not occur for this target. The individual $CoNi_2O_4$ target was mixed from NiO and Co_3O_4 powders. It was manually milled for an hour before being pressed and sintered at 1200 °C for 10 h.

All of the thin-film samples were made with a pulsed laser deposition (PLD) system and a KrF excimer laser (Lambda Physik, λ = 248 nm) with a laser energy of 500 mJ. A deposition temperature of 850 °C, a background pressure of 100 mTorr O_2, and a pulse number of 5000 were used for each deposition at both 2 and 10 Hz on STO

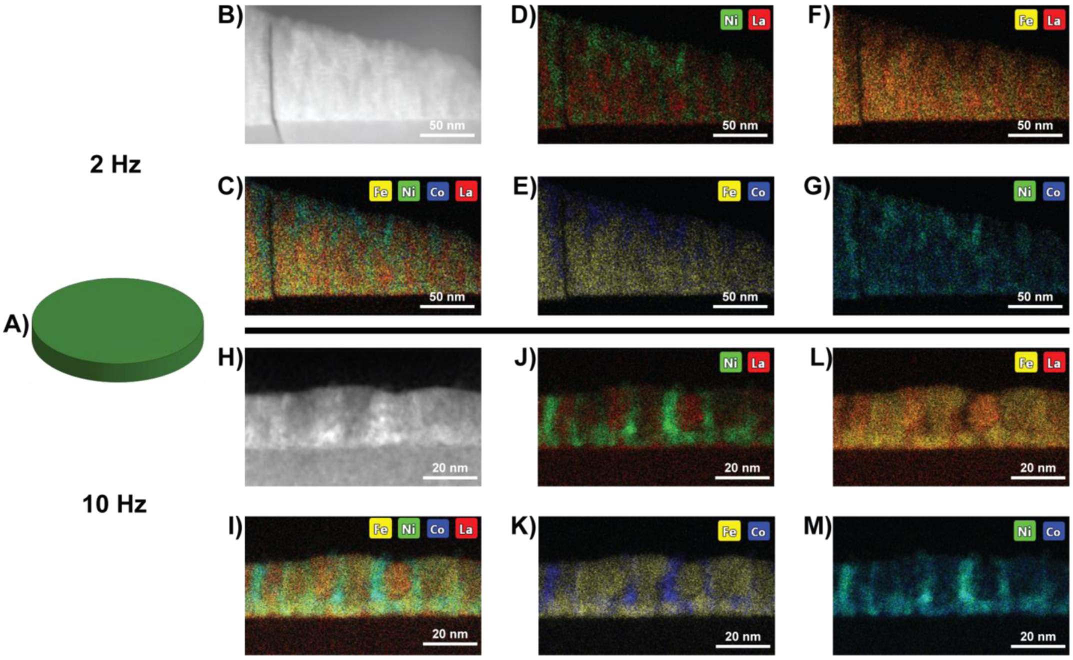

Figure 2. (A) Schematic of the combined target. For the 2 Hz sample: (B) STEM, (C) EDS of La, Co, Ni, and Fe combined, (D) EDS of La and Ni combined, (E) EDS of Co and Fe combined, (F) EDS of La and Fe combined, and (G) EDS of Co and Ni combined. For the 10 Hz sample: (H) STEM, (I) EDS of La, Co, Ni, and Fe combined, (J) EDS of La and Ni combined, (K) EDS of Co and Fe combined, (L) EDS of La and Fe combined, and (M) EDS of Co and Ni combined.

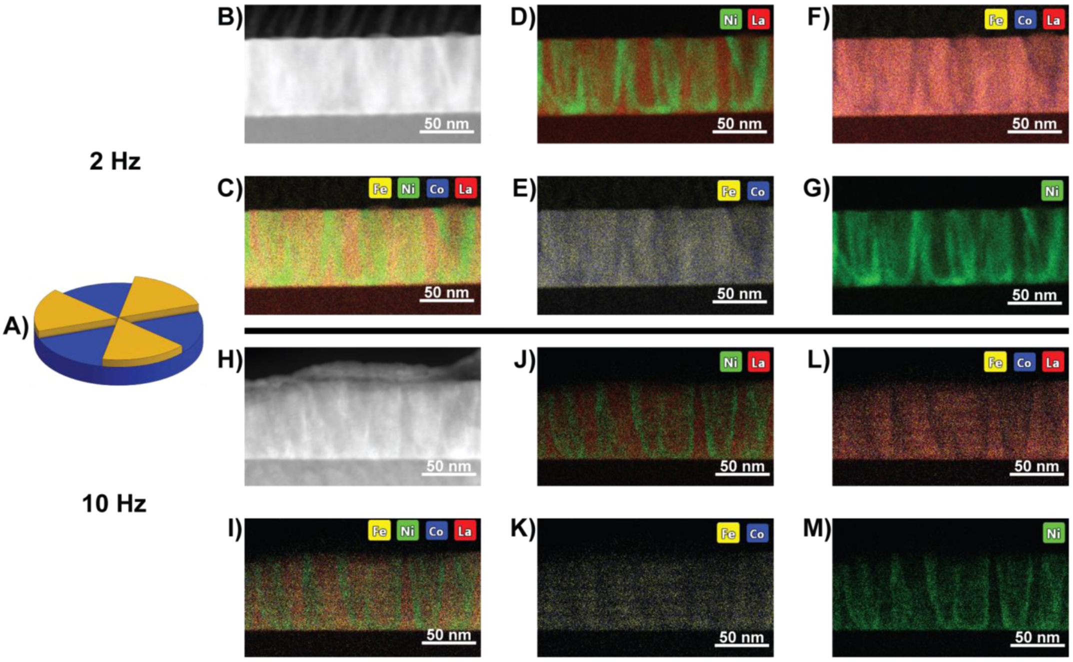

Figure 3. (A) Schematic of the pie-shaped target. For the 2 Hz sample: (B) STEM, (C) EDS of La, Co, Ni, and Fe combined, (D) EDS of La and Ni combined, (E) EDS of Co and Fe combined, (F) EDS of La, Co, and Fe combined, and (G) EDS of Ni by itself. For the 10 Hz sample: (H) STEM, (I) EDS of La, Co, Ni, and Fe combined, (J) EDS of La and Ni combined, (K) EDS of Co and Fe combined, (L) EDS of La, Co, and Fe combined, and (M) EDS of Ni by itself.

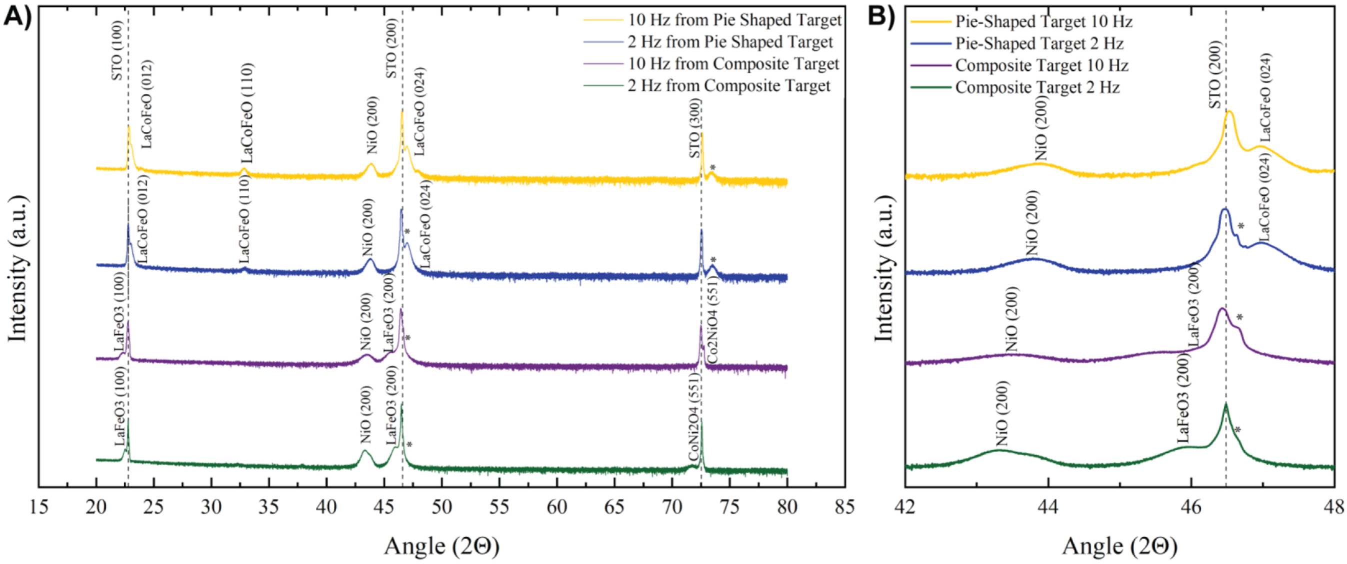

Figure 4. (A) XRD θ−2θ scan depicting the various deposition parameters on the STO (001) substrate and a (B) detailed XRD θ−2θ scan from 42° to 48°.

(100) substrates. 5 Hz samples were also made, with their XRD, TEM, magnetism, and optical data in the Supporting Information. After deposition, the samples were cooled to room temperature at a rate of 15 °C/min under a background pressure of 100 mTorr O_2. The samples were then cut into roughly 5 × 5 mm wide pieces.

Crystallinity, elemental, and microstructural characterizations were performed with a PANalytical Empyrean XRD and high-resolution Thermo Fisher Scientific TALOS F200X STEM operated at 200 kV. Sample preparation was carried out by thinning the sample through manual grinding and polishing followed by dimpling and more polishing. The sample was then finished with a PIPS II model 695 ion miller from Gatan.

Magnetic measurements were completed with an MPMS model 3 (Quantum Design). The magnetic moment versus applied field measurement was completed in both the in-plane and out-of-plane direction at 300 and 10 K to a field of 70 kOe. The magnetic moment versus temperature measurements were carried out in the out-of-plane direction with an applied field of 1−2 T, depending on the needs of each film. The dielectric permittivity for each film was measured using angular-dependent spectroscopic ellipsometry on a J.A. Woollam RC2 ellipsometer. The parameters psi (Ψ) and delta (Δ) were collected at 55°, 65°, and 75° from 500 to 1500 nm. CompleteEASE was used to fit the ellipsometer parameters with a uniaxial general oscillator model.

■ RESULTS AND DISCUSSION

The four samples were deposited at either 2 or 10 Hz for the composite and pie-shaped targets. All samples were expected to form films of LFO−CNO VAN systems, as shown in the schematic drawing in Figure 1. The cross-sectional STEM and EDS results can be seen in Figures 2 and 3 for the composite (i.e., mixed) and pie-shaped target samples, respectively. The cross-sectional STEM/EDS images confirm that the VAN structure has formed for both target configurations, with the pie-shaped target case presenting a more obvious VAN structure. A careful examination of the EDS images (parts C-E for 2 Hz and parts I−K for 10 Hz) reveals that the composite target films formed the expected LFO matrix with CNO nanopillars, and the pie-shaped target films formed a new system: LaCoFeO (LCFO) matrix with NiO nanopillars. Examining Figures 2 and 3 parts D and E for the 2 Hz samples and parts J and K for the 10 Hz samples allows for the separation of the four elements (i.e., La, Ni, Co, and Fe) to be easily seen. It is clear that the samples deposited using the pie-shaped target in Figure 3 have a different mapping than the composite target samples in Figure 2, and this shows that two different morphologies were made using the different targets. The XRD results from Figure 4 also suggest that the XRD peaks also matched with the materials seen in the EDS mapping. In addition, pillars in a VAN system usually contain less material than the matrix and thus will result in lower peak intensity. By observing the XRD results and the peak intensities with respect to each other, the pillars were determined to be CNO in the composite target samples and NiO in the pie-shaped target samples. Based on these results, Figures 2 and 3 are updated in parts F and G for the 2 Hz samples and parts L and M for the 10 Hz sample to represent the final microstructure. The oxygen EDS mapping results provided in Figures S1 and S2 show that oxygen is represented throughout the full film. The difference in the pie-shaped target is believed to result from two phenomena: the target sintering conditions and the plasma plume interactions during the film deposition. In the composite target, all the materials are allowed to react during target sintering, yielding a different chemistry in this target when compared to the pie-shaped target. Additionally, the high-energy adatoms in the laser plume from the composite target can react before reaching the substrate. This is not the case in the pie-shaped target, where the plume only contains one composition at a time (i.e., LFO or CNO); therefore, all material mixing could only occur during the adatom diffusion process on the substrate. The extra energy from the PLD deposition could allow the cobalt oxide adatoms to mix with the LFO, resulting in different material phases.

From the TEM and EDS data, the film thickness and pillar diameters were calculated for each sample and are summarized in Table 1. This measurement was carried out by averaging the thickness from multiple points on the STEM images. The samples made from the pie-shaped target had a consistent thickness when compared to each other, but the samples made from the composite target displayed a considerable thickness variation. The pillar diameter was seen to increase with increasing film thickness, though not significantly except for the thinnest film having the thinnest pillars. This suggests that the film was not able to grow to an adequate thickness for larger pillars to form. The pillar thickness measurement was carried out by measuring the thickness of multiple different pillars along their length in the lanthanum−nickel EDS images, where the element separation is most prevalent.

Table 1. Film Thickness and Pillar Diameter Data for Both Target Types at Both 2 and 10 Hz Deposition Frequencies

	frequency (Hz)	film thickness (nm)	film thickness error (nm)	pillar diameter (nm)	pillar diameter error (nm)
composite target	2	128.82	6.09	6.42	1.75
	10	21.93	2.23	3.89	1.82
pie-shaped target	2	72.96	1.04	5.66	2.03
	10	73.63	5.08	6.25	1.99

XRD data were collected to confirm the film composition, as shown in Figure 4A. Similar to the results in the STEM/EDS data in Figures 2 and 3, the composite target showed LFO and CNO peaks, while the pie-shaped target showed LCFO and NiO peaks. As seen in Figure 4B, the LFO (200) peak for the sample made from the composite target at 10 Hz was highly strained, offsetting by 0.8°. It is also important to note that a minor and broad NiO peak is present in all four films, despite the fact that only the pie-shaped target film showed clear NiO pillars in the EDS data. Figure 4B indicates that the NiO peaks in the two composite target films are also highly strained, showing that NiO is not an optimal material for growth in those films.

The two different target configurations resulted in different VAN phases and morphologies, which could also result in distinct properties; therefore, we conducted a set of magnetic measurements to examine possible tunability with this method. Magnetic hysteresis loops were measured for all of the samples. In the case of the composite target samples, the ferrimagnetic pillars of CNO are inside a FM LFO matrix. However, the pie-shaped target has AFM NiO pillars in an FM LCFO matrix. Figure 5 presents the hysteresis loops collected for all four samples at both 300 and 10 K, showing distinctive results. The composite target films in Figure 5A,B for 300 and 10 K depict a strong magnetic response, while the pie-shaped target in Figure 5C,D, at the same temperatures, shows a weak magnetic response. Figure 5E,F shows the enlarged plots marked in 5C and 5D. It is apparent that the composite target resulted in an LFO−CNO VAN which contains very strong out-of-plane (OP) magnetic anisotropy for both 2 and 10 Hz samples. Table 2 summarizes the coercive field (Hc) and saturation magnetization (Ms) of all the samples for both the in-plane (IP) and OP measurements at both 300 and 10 K. Analysis of Table 2 reveals that the saturation, averaged across temperatures, is nearly an order of magnitude larger for the composite target films when compared to the pie-shaped target films in both the IP and OP directions. Conversely, the coercivity showed more substantial differences with the composite targets in the IP direction being 30 times larger than the pie-shaped samples and the OP direction being 2 orders of magnitude larger.

To fully understand the underlying mechanisms, it is crucial to revisit the composition of each film. The films made from the composite target have an FM LFO matrix and ferrimagnetic CNO pillars. CNO has unique lattices that contain two different magnetic sublattices (CoO_2 and NiO) and can often result in a larger coercivity and saturation when compared to other FM materials. For the samples from the pie-shaped target, the weak magnetization suggests little to no exchange bias coupling between the FM/AFM phases. The

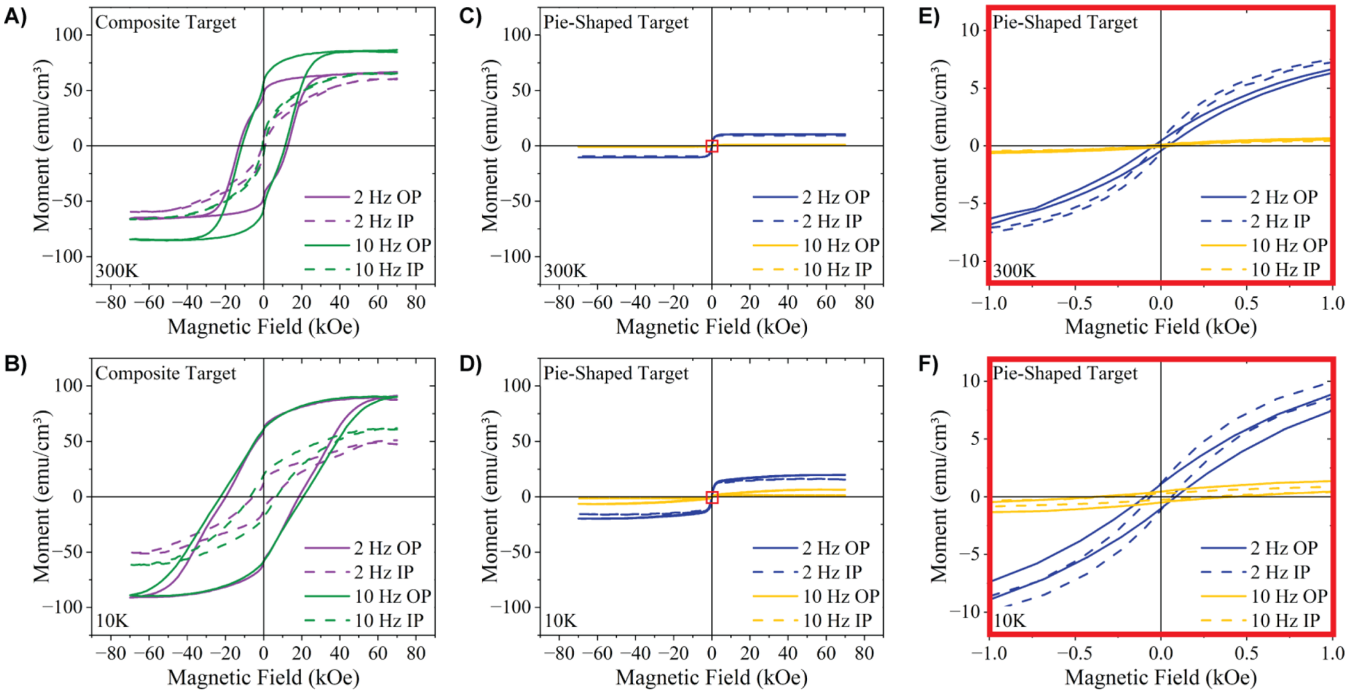

Figure 5. Magnetic moment versus magnetic field at (A) 300 K for the composite target samples, (B) 10 K for the composite target, (C) 300 K for the pie-shaped target, (D) 10 K for the pie-shaped target, (E) 300 K inset for the pie-shaped target, and (F) 10 K inset for the pie-shaped target.

Table 2. Magnetic Properties for Both Target Types at Both 2 and 10 Hz Deposition Frequencies

			coercivity (Oe)	saturation (emu/cm^3)
composite 2 Hz	300 K	OP	12.79	68.33
		IP	80.20×10^{-2}	60.40
	10 K	OP	19.18	88.78
		IP	5.25	50.30
composite 10 Hz	300 K	OP	11.36	85.58
		IP	61.10×10^{-2}	65.37
	10 K	OP	21.69	90.62
		IP	6.94	61.19
pie-shaped 2 Hz	300 K	OP	4.04×10^{-2}	10.42
		IP	2.90×10^{-2}	9.27
	10 K	OP	8.91×10^{-2}	19.75
		IP	6.30×10^{-2}	15.59
pie-shaped 10 Hz	300 K	OP	6.26×10^{-2}	96.25×10^{-2}
		IP	8.10×10^{-2}	68.32×10^{-2}
	10 K	OP	40.22×10^{-2}	6.40
		IP	30.54×10^{-2}	1.35

film contains larger yet fewer pillars, which limit the interfaces where these interactions occur. Instead, the AFM pillars became dominant during the measurement, as demonstrated by the extremely weak hysteresis loop. For the 2 Hz pie-shaped sample, the FM matrix might contribute to the magnetic response, but the AFM pillars still dominated the film's response. The difference between the four films made from two different target configurations is interesting and results in very different magnetic properties, despite starting with the same elements in two different configurations.

Optical spectroscopic ellipsometry was used to explore the optical permittivity, a measure of how materials respond to light and how the light is propagated throughout the material, and the optical anisotropy, which occurs from the permittivity values being different in the IP (i.e., parallel to the film) and OP direction (i.e., perpendicular to the film). This is represented by the permittivity plots shown in Figure 6. All films showed obvious optical anisotropy, indicated by the significantly different permittivities between the IP and OP directions for all four films deposited. In Figure 6A, the composite target exhibited higher IP permittivity than that of OP, while the pie-shaped target in Figure 6B displayed higher OP permittivity than that of IP. The composite films, containing conducting pillars (CNO) embedded in a Mott insulating matrix (LFO), show a higher IP permittivity due to the alignment and density of the conducting pillars in the vertical direction, which results in lower charge carrier density and a higher permittivity in-plane.[30−32] The composite 2 Hz sample having larger pillars, as shown in Table 1, has a greater IP permittivity compared to the composite 10 Hz sample due to the charge carrier density within the conducting pillars and the unique properties of the Mott insulator and its electron—electron bonds. Conversely, the pie-shaped target formed semiconducting pillars (NiO) and a semiconducting matrix (LCFO), where the charge carriers are distributed more in the matrix in-plane considering the slightly higher conductivity in LCFO than that of NiO, and thus result in lower IP permittivity. Here, there are thicker NiO pillars in the pie-shaped 2 Hz sample than those in the 10 Hz sample, explaining why the pie-shaped 2 Hz sample presents a higher OP permittivity compared to the 10 Hz sample. Despite originating from the same starting materials, the samples made from the two different target configurations exhibited widely diverging properties which can be attributed to the distinct electronic and structural morphologies in the films which influence the optical behaviors, as supported by the magnetic data. Supporting Information containing the imaginary permittivity data can be found in Figure S3.

No prior work has specifically been carried out on the LFO—CNO-based VANs, though similar studies do exist in the

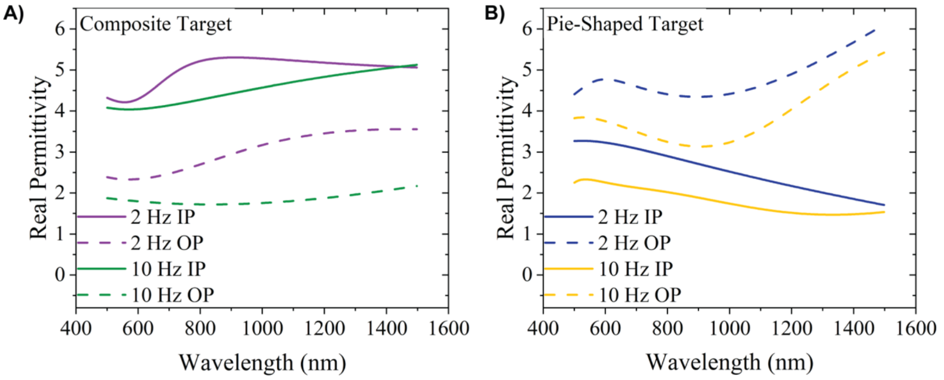

Figure 6. Optical properties of (A) composite target samples and (B) pie-shaped target samples.

literature. One example is the sol−gel deposition of $LaNiO_3$−$CoFe_2O_4$ (LNO−CFO), which displayed a saturation magnetization that fell between that of the composite target samples and pie-shaped target samples in this study.[31−33] It is interesting to note that our films result in LFO−CNO, instead of LNO−CFO processed by the sol−gel method. Another example, also using the sol−gel method, includes the deposition of $LaFeO_3$−$CoFe_2O_4$ (LFO−CFO) systems due to the system's high exchange-coupling and magnetic coercivity.[34−36] Neither composition produced a continuous thin film or the unique VAN morphology, but this does show that there is interest in this type of composite magnetic thin films. The strong FM responses, unique magnetic anisotropy, and optical anisotropy found in the samples in this work suggest that the new LFO−CNO VAN system could find unique applications in magnetic data storage, optical devices, and spintronics. The demonstration on target configuration tuning could also be applied to many other VAN systems and provide a new design degree-of-freedom beyond the typical growth parameters tuned during deposition.[37,38]

CONCLUSIONS

In this work, two different target configuration methods were used to explore the target configuration and its impact on LFO−CNO VAN growth and their properties. Despite using the same deposition conditions, these two different target configurations formed different film morphologies with widely varying magnetic and optical properties. The composite target formed films featuring an LFO matrix and CNO pillars are hard magnetic materials and have strong optical anisotropy. Conversely, the pie-shaped target formed films consisting of a LCFO matrix and NiO pillars are weak magnetic materials but much stronger out-of-plane optical anisotropy. These findings show that the VAN microstructures are sensitive to target composition and morphology, suggesting target configuration as a vital method to tune the material characteristics. Future work can explore the potential of different target configurations to determine whether they form more unique microstructures. This study shows valuable insights into the relationship among target configurations, microstructures, and properties in VANs.

ASSOCIATED CONTENT

Supporting Information

The Supporting Information is available free of charge at https://pubs.acs.org/doi/10.1021/acs.cgd.4c00958.

TEM, STEM, and single-element EDS images for the composite samples at 2 and 10 Hz; TEM, STEM, and single-element EDS images for the pie-shaped samples at 2 and 10 Hz; imaginary optical properties for the composite and pie-shaped samples at 2 and 10 Hz; TEM, STEM, and EDS images for the composite sample at 5 Hz; TEM, STEM, and EDS images for the pie-shaped sample at 5 Hz; film thickness and pillar diameter data for the composite and pie-shaped samples at 5 Hz; XRD θ−2θ scans for the composite and pie-shaped samples at 5 Hz; magnetic moment versus magnetic field for the composite and pie-shaped samples at 5 Hz; magnetic properties for the composite and pie-shaped samples at 5 Hz; and real and imaginary optical properties for the composite and pie-shaped targets at 5 Hz (PDF)

AUTHOR INFORMATION

Corresponding Author

Haiyan Wang − *School of Materials Engineering, Purdue University, West Lafayette, Indiana 47907, United States; School of Electrical and Computer Engineering, Purdue University, West Lafayette, Indiana 47907, United States;* orcid.org/0000-0002-7397-1209; Email: hwang00@purdue.edu

Authors

Lizabeth Quigley − *School of Materials Engineering, Purdue University, West Lafayette, Indiana 47907, United States;* orcid.org/0000-0002-8691-8992
Jianan Shen − *School of Materials Engineering, Purdue University, West Lafayette, Indiana 47907, United States;* orcid.org/0000-0003-3226-2761
Juanjuan Lu − *School of Materials Engineering, Purdue University, West Lafayette, Indiana 47907, United States;* orcid.org/0000-0003-4885-8287
Claire A. Mihalko − *School of Materials Engineering, Purdue University, West Lafayette, Indiana 47907, United States*
James P. Barnard − *School of Materials Engineering, Purdue University, West Lafayette, Indiana 47907, United States;* orcid.org/0000-0002-7570-952X
Yizhi Zhang − *School of Materials Engineering, Purdue University, West Lafayette, Indiana 47907, United States*
Nirali A. Bhatt − *School of Materials Engineering, Purdue University, West Lafayette, Indiana 47907, United States*
Katrina Evancho − *School of Materials Engineering, Purdue University, West Lafayette, Indiana 47907, United States*
Raktim Sarma − *Sandia National Laboratory, Albuquerque, New Mexico 87185, United States; Center for Integrated*

Nanotechnologies, Sandia National Laboratory, Albuquerque, New Mexico 87185, United States

Aleem Siddiqui − *Sandia National Laboratory, Albuquerque, New Mexico 87185, United States; Center for Integrated Nanotechnologies, Sandia National Laboratory, Albuquerque, New Mexico 87185, United States*

Complete contact information is available at: https://pubs.acs.org/10.1021/acs.cgd.4c00958

Author Contributions

The manuscript was written through contributions of all authors. All authors have given approval to the final version of the manuscript. Lizabeth Quigley prepared the manuscript and worked on PLD deposition, XRD characterization, magnetic characterization, and TEM sample preparation. Jianan Shen assisted PLD depositions and TEM imaging. Juanjuan Lu conducted TEM imaging. Claire A. Mihalko contributed to some of the ellipsometry measurements. James P. Barnard conducted part of the TEM imaging. Yizhi Zhang conducted part of the TEM imaging. Nirali A. Bhatt assisted with some of the ellipsometry images. Katina Evancho participated in TEM sample preparation. Raktim Sarma assisted in providing research direction. Aleem Siddiqui assisted in providing research direction. Haiyan Wang acquired the research funding, conceived the research project, guided the research, and revised the manuscript.

Notes

The authors declare no competing financial interest.

■ ACKNOWLEDGMENTS

This work is supported by the U.S. Department of Energy, Office of Science, Basic Energy Sciences under Award DE-SC0020077. Part of this work was performed at the Center for Integrated Nanotechnologies, an Office of Science User Facility and operated by the U.S. Department of Energy (DOE) Office of Science and performed under the Laboratory Directed Research and Development (LDRD) program at the Sandia National Laboratories. Sandia National Laboratories is a multimission laboratory managed and operated by National Technology & Engineering Solutions of Sandia, LLC, a wholly owned subsidiary of Honeywell International Inc., for the U.S. Department of Energy's National Nuclear Security Administration under contract DE-NA0003525. This article describes objective technical results and analysis. Any subjective views or opinions that might be expressed in the article do not necessarily represent the views of the U.S. Department of Energy or the United States Government. Additionally, this work was partially supported by the Sandia National Laboratories Diversity Initiative Fellowship (L.Q. and N.A.B.). Y.Z. acknowledges the support by the U.S. National Science Foundation (DMR-2016453, high-resolution STEM work). N.A.B. acknowledges the partial support from the Purdue University Andrews Graduate Fellowship. L.Q. thanks the partial support from the Purdue University Doctoral Graduate Fellowship.

■ REFERENCES

(1) Chen, A.; Jia, Q. A Pathway to Desired Functionalities in Vertically Aligned Nanocomposites and Related Architectures. *MRS Bull.* **2021**, *46* (2), 115−122.

(2) Misra, S.; Wang, H. Review on the growth, properties and applications of self-assembled oxide−metal vertically aligned nanocomposite thin films—current and future perspectives. *Mater. Horiz.* **2021**, *8*, 869−884.

(3) Zhang, W.; Chen, A.; Bi, Z.; Jia, Q.; MacManus-Driscoll, J. L.; Wang, H. Interfacial Coupling in Heteroepitaxial Vertically Aligned Nanocomposite Thin Films: From Lateral to Vertical Control. *Curr. Opin. Solid State Mater. Sci.* **2014**, *18* (1), 6−18.

(4) Wang, X.; Wang, H. Recent Advances in Vertically Aligned Nanocomposites with Tunable Optical Anisotropy: Fundamentals and Beyond. *Chemosensors* **2021**, *9* (6), 145.

(5) Huang, J.; MacManus-Driscoll, J. L.; Wang, H. New Epitaxy Paradigm in Epitaxial Self-Assembled Oxide Vertically Aligned Nanocomposite Thin Films. *J. Mater. Res.* **2017**, *32* (21), 4054−4066.

(6) Basov, S.; Elissalde, C.; Simon, Q.; Maglione, M.; Castro-Chavarria, C.; de Beauvoir, T. H.; Payan, S.; Temst, K.; Lazenka, V.; Andrei Antohe, V.; de Sá, P. M. P.; Sallagoity, D.; Piraux, L. Simple Synthesis and Characterization of Vertically Aligned Ba$_{0.7}$Sr$_{0.3}$TiO$_3$−CoFe$_2$O$_4$ Multiferroic Nanocomposites from CoFe$_2$ Nanopillar Arrays. *Nanotechnology* **2017**, *28* (47), 475707.

(7) Zhang, B.; Huang, J.; Rutherford, B. X.; Lu, P.; Misra, S.; Kalaswad, M.; He, Z.; Gao, X.; Sun, X.; Li, L.; Wang, H. T. Room-Temperature Multiferroic Fe-BaTiO$_3$ Vertically Aligned Nanocomposites with Perpendicular Magnetic Anisotropy. *Mater. Today Nano* **2020**, *11*, 100083.

(8) Zhang, W.; Jian, J.; Chen, A.; Jiao, L.; Khatkhatay, F.; Li, L.; Chu, F.; Jia, Q.; MacManus-Driscoll, J. L.; Wang, H. Strain relaxation and enhanced perpendicular magnetic anisotropy in BiFeO$_3$:CoFe2O$_4$ vertically aligned nanocomposite thin films. *Appl. Phys. Lett.* **2014**, *104*, 062402.

(9) Zhang, W.; Chen, A.; Jian, J.; Zhu, Y.; Chen, L.; Lu, P.; Jia, Q.; MacManus-Driscoll, J. L.; Zhang, X.; Wang, H. Strong Perpendicular Exchange Bias in Epitaxial La$_{0.7}$Sr$_{0.3}$MnO$_3$:BiFeO$_3$ Nanocomposite Films through Vertical Interfacial Coupling. *Nanoscale* **2015**, *7* (33), 13808−13815.

(10) Lu, J.; Zhang, D.; Paldi, R. L.; He, Z.; Lu, P.; Deitz, J.; Ahmad, A.; Dou, H.; Wang, X.; Liu, J.; Hu, Z.; Yang, B.; Zhang, X.; El-Azab, A. A.; Wang, H. Abnormal In-Plane Epitaxy and Formation Mechanism of Vertically Aligned Au Nanopillars in Self-Assembled CeO$_2$−Au Metamaterial Systems. *Mater. Horiz.* **2023**, *10* (8), 3101−3113.

(11) Huang, J.; Li, L.; Lu, P.; Qi, Z.; Sun, X.; Zhang, X.; Wang, H. Self-Assembled Co−BaZrO$_3$ Nanocomposite Thin Films with Ultra-Fine Vertically Aligned Co Nanopillars. *Nanoscale* **2017**, *9* (23), 7970−7976.

(12) Zhang, W.; Chen, A.; Khatkhatay, F.; Tsai, C.-F.; Su, Q.; Jiao, L.; Zhang, X.; Wang, H. Integration of Self-Assembled Vertically Aligned Nanocomposite (La$_{0.7}$Sr$_{0.3}$MnO$_3$)$_{1-x}$:(ZnO)$_x$ Thin Films on Silicon Substrates. *ACS Appl. Mater. Interfaces* **2013**, *5* (10), 3995.

(13) Bhatt, N. A.; Paldi, R. L.; Barnard, J. P.; Lu, J.; He, Z.; Yang, B.; Shen, C.; Song, J.; Sarma, R.; Siddiqui, A.; Wang, H. ZnO-Au Hybrid Metamaterial Thin Films with Tunable Optical Properties. *Crystals* **2024**, *14* (1), 65.

(14) Chen, A.; Weigand, M.; Bi, Z.; Zhang, W.; Lü, X.; Dowden, P.; MacManus-Driscoll, J. L.; Wang, H.; Jia, Q. Evolution of Microstructure, Strain and Physical Properties in Oxide Nanocomposite Films. *Sci. Rep.* **2014**, *4* (1), 5426.

(15) Wang, X.; Nguyen, T.; Cao, Y.; Jian, J.; Malis, O.; Wang, H. AlN-Based Hybrid Thin Films with Self-Assembled Plasmonic Au and Ag Nanoinclusions. *Appl. Phys. Lett.* **2019**, *114* (2), 023103.

(16) Kim, T. C.; Lee, S. H.; Jung, H. K.; Kim, Y. E.; Choi, J. W.; Yang, D.; Kim, D. H. Effect of Sputtering Conditions on the Structure and Magnetic Properties of Self-Assembled BiFeO$_3$-CoFe$_2$O$_4$ Nanocomposite Thin Films. *J. Magn. Magn. Mater.* **2019**, *471*, 116−123.

(17) Huang, J.; Wang, X.; Hogan, N. L.; Wu, S.; Lu, P.; Fan, Z.; Dai, Y.; Zeng, B.; Starko-Bowes, R.; Jian, J.; Wang, H.; Li, L.; Prasankumar, R. P.; Yarotski, D.; Sheldon, M.; Chen, H.-T.; Jacob, Z.; Zhang, X.; Wang, H. Nanoscale Artificial Plasmonic Lattice in Self-Assembled Vertically Aligned Nitride−Metal Hybrid Metamaterials. *Adv. Sci.* **2018**, *5* (7), 1800416.

(18) Wang, X.; Jian, J.; Diaz-Amaya, S.; Kumah, C. E.; Lu, P.; Huang, J.; Lim, D. G.; Pol, V.; Youngblood, J. P.; Boltasseva, A.;

Stanciu, L. A.; O'Carroll, D. M.; Zhang, X.; Wang, H. Hybrid Plasmonic Au−TiN Vertically Aligned Nanocomposites: A Nanoscale Platform towards Tunable Optical Sensing. *Nanoscale Adv.* **2019**, *1* (3), 1045−1054.

(19) Wang, H.; Cui, M.; Fu, G.; Zhang, J.; Ding, X.; Azaceta, I.; Bugnet, M.; Kepaptsoglou, D. M.; Lazarov, V. K.; de la Peña O'Shea, V. A.; Oropeza, F. E.; Zhang, K. H. L. Vertically Aligned Ni/NiO Nanocomposites with Abundant Oxygen Deficient Hetero-Interfaces for Enhanced Overall Water Splitting. *Sci. China Chem.* **2022**, *65* (10), 1885−1894.

(20) Hu, Z.; Lu, J.; Dou, H.; Shen, J.; Barnard, J. P.; Liu, J.; Zhang, X.; Wang, H. Template-Assisted Growth of Co-$BaTiO_3$ Vertically Aligned Nanocomposite Thin Films with Strong Magneto-Optical Coupling Effect. *Nano Res.* **2024**, *17* (4), 3130−3138.

(21) Rutherford, B. X.; Zhang, D.; Quigley, L.; Barnard, J. P.; Yang, B.; Lu, J.; Kunwar, S.; Dou, H.; Shen, J.; Chen, A.; Wang, H. Combinatorial Growth of Vertically Aligned Nanocomposite Thin Films for Accelerated Exploration in Composition Variation. *Small Sci.* **2023**, *3* (11), 2300049.

(22) Panchal, G.; Panchwanee, A.; Kumar, M.; Fritsch, K.; Choudhary, R. J.; Phase, D. M. Synthesis and Characterization of Vertically Aligned $La_{0.7}Sr_{0.3}MnO_3$:NiO Nanocomposite Thin Films for Spintronic Applications | ACS Applied Nano Materials. *ACS Applied Nanomaterials* **2021**, *4*, 102.

(23) Song, J.; Zhang, D.; Lu, P.; Wang, H.; Xu, X.; Meyerson, M. L.; Rosenberg, S. G.; Deitz, J.; Liu, J.; Wang, X.; Zhang, X.; Wang, H. Anisotropic Optical and Magnetic Response in Self-Assembled TiN−$CoFe_2$ Nanocomposites. *Mater. Today Nano* **2023**, *22*, 100316.

(24) Wang, X.; Jian, J.; Wang, H.; Liu, J.; Pachaury, Y.; Lu, P.; Rutherford, B. X.; Gao, X.; Xu, X.; El-Azab, A.; Zhang, X.; Wang, H. Nitride-Oxide-Metal Heterostructure with Self-Assembled Core−Shell Nanopillar Arrays: Effect of Ordering on Magneto-Optical Properties. *Small* **2021**, *17* (5), 2007222.

(25) Wang, X.; Wang, H.; Jian, J.; Rutherford, B. X.; Gao, X.; Xu, X.; Zhang, X.; Wang, H. Metal-Free Oxide-Nitride Heterostructure as a Tunable Hyperbolic Metamaterial Platform. *Nano Lett.* **2020**, *20*, 6614.

(26) Horton, M. K.; Montoya, J. H.; Liu, M.; Persson, K. A. High-Throughput Prediction of the Ground-State Collinear Magnetic Order of Inorganic Materials Using Density Functional Theory. *Npj Comput. Mater.* **2019**, *5* (1), 64.

(27) Jain, A.; Ong, S. P.; Hautier, G.; Chen, W.; Richards, W. D.; Dacek, S.; Cholia, S.; Gunter, D.; Skinner, D.; Ceder, G.; Persson, K. A. Commentary: The Materials Project: A Materials Genome Approach to Accelerating Materials Innovation. *APL Mater.* **2013**, *1* (1), 011002.

(28) Alsulami, R. M.; Alzeer, R. S.; Aloqaili, S. S.; Alruwashid, F. S. Synthesis and Characterization of CoX_2O_4 Nanostructured Oxides. *Results Mater.* **2023**, *18*, 100392.

(29) Prasad, P.; Sivanandan, V. T.; Prasad, A. S. Room Temperature Ferromagnetic Behavior of Nanocrystalline $LaFeO_3$ Perovskite Oxide Synthesized Through Phytochemical Mediated Combustion Technique. *J. Clust. Sci.* **2024**, *35* (3), 929−940.

(30) Kumar Das, M.; Panda, S.; Mohapatra, N. Power Conversion Efficiency Optimization of $LaFeO_3$ Mott Insulator Based Solar Cell with Metal Oxide Transport Layers Using SCAPS. *Mater. Today Proc.* **2023**, *74*, 756−762.

(31) Ruppen, J.; Teyssier, J.; Peil, O. E.; Catalano, S.; Gibert, M.; Mravlje, J.; Triscone, J.-M.; Georges, A.; van der Marel, D. Optical Spectroscopy and the Nature of the Insulating State of Rare-Earth Nickelates. *Phys. Rev. B* **2015**, *92* (15), 155145.

(32) Omori, Y.; Rüegg, A.; Sigrist, M. Electrical Permittivity Driven Metal-Insulator Transition in Heterostructures of Nonpolar Mott and Band Insulators. *Phys. Rev. B* **2014**, *90* (15), 155118.

(33) Patra, A.; Maity, K. P.; Prasad, V. Influence of Orbital Two-Channel Kondo Effect on Anomalous Hall Effect in Ferrimagnetic Composites of $LaNiO_3$ and $CoFe_2O_4$. *J. Phys.: Condens. Matter* **2019**, *31* (25), 255702.

(34) Patra, A.; Maity, K. P.; Kamble, R. B.; Prasad, V. Tuning Spin One Channel to Exotic Orbital Two-Channel Kondo Effect in Ferrimagnetic Composites of $LaNiO_3$ and $CoFe_2O_4$. *J. Phys.: Condens. Matter* **2018**, *30* (37), 375701.

(35) Patra, A.; Prasad, V. Effect of LaNiO3 on the Impedance and Dielectric Properties of $CoFe_2O_4$: A High Temperature Study. *J. Phys. Appl. Phys.* **2020**, *53* (4), 045301.

(36) Sayed, F.; Kotnana, G.; Barucca, G.; Muscas, G.; Peddis, D.; Mathieu, R.; Sarkar, T. $LaFeO_3$-$CoFe_2O_4$ Bi-Magnetic Composite Thin Films Prepared Using an All-in-One Synthesis Technique. *J. Magn. Magn. Mater.* **2020**, *503*, 166622.

(37) Sharma, P.; Jain, A.; Chatterjee, R. Enhanced Magnetic Performance in Exchange-Coupled $CoFe_2O_4$−$LaFeO_3$ Nanocomposites. *Nanotechnology* **2022**, *33* (10), 105708.

(38) Velaga, M.; Pani, J.; Rao, B. M.; Gaikwad, V. M.; Borkar, H. Exploring Hydrogen Evolution in Perovskite $LaFeO_3$ and Composites with Spinel Ferrite $CoFe_2O_4$. *J. Mater. Sci. Mater. Electron.* **2024**, *35* (14), 980.